arXiv:1610.03407v1 [astro-ph.SR] 11 Oct 2016

1.3 MM POLARIZED EMISSION IN THE CIRCUMSTELLAR DISK OF A MASSIVE PROTOSTAR

M. FERNÁNDEZ-LÓPEZ[1], I. W. STEPHENS[2,3], J. M. GIRART[4,3], L. LOONEY[5], S. CURIEL[6], D. SEGURA-COX[5], C. ESWARAIAH[7], AND S.-P. LAI [7]

Draft version October 12, 2016

ABSTRACT

We present the first resolved observations of the 1.3 mm polarized emission from the disk-like structure surrounding the high-mass protostar Cepheus A HW2. These CARMA data partially resolve the dust polarization, suggesting an uniform morphology of polarization vectors with an average position angle of $57° \pm 6°$ and an average polarization fraction of $2.0\% \pm 0.4\%$. The distribution of the polarization vectors can be attributed to (1) the direct emission of magnetically aligned grains of dust by a uniform magnetic field, or (2) the pattern produced by the scattering of an inclined disk. We show that both models can explain the observations, and perhaps a combination of the two mechanisms produce the polarized emission. A third model including a toroidal magnetic field does not match the observations. Assuming scattering is the polarization mechanism, these observations suggest that during the first few 10^4 years of high-mass star formation, grain sizes can grow from 1 μm to several 10s μm.

Subject headings: ISM: individual objects (Cepheus A HW2) – ISM: magnetic fields – polarization – stars: formation – techniques: polarimetric

1. INTRODUCTION

Recently, polarization has been resolved in a few circumstellar disks around low-mass protostars via millimeter and centimeter radio-interferometric observations. Specifically, these resolved polarization detections were found for two Class 0 sources (IRAS 16293-2422 and L1527, Rao et al. 2014; Segura-Cox et al. 2015) and a Class I/II source (HL Tauri Stephens et al. 2014). A fourth detection has been reported toward the candidate disk of the Class 0 protostar NGC1333 IRAS4A1 (Cox et al. 2015). However, these observations have a small number of independent polarization measurements difficulting to discern the nature of the polarized emission.

Usually, the polarized (sub)millimeter continuum emission from protostellar disks has been interpreted as a consequence of the presence of a magnetic field (although see discussions about other possibilities in Gold 1952a,b; Andersson et al. 2015). The short axis of dust grains preferentially aligns with the magnetic field causing dust polarization to be perpendicular with the magnetic field (Lazarian 2007; Andersson et al. 2015, and references therein). This polarization mechanism is ex-

pected to dominate dust emission at scales larger than the disk, and is frequently used by interferometers to investigate the role of magnetic fields at the envelope scale (e.g., Rao et al. 1998; Girart et al. 1999, 2006, 2009; Stephens et al. 2013). However, this mechanism is not the only way of producing (sub)millimeter polarized emission. Dust grain growth is expected to happen in protostellar disks (Beckwith et al. 2000; Testi et al. 2014). Scattering by large enough dust grains ($\gtrsim 10$ μm) may also cause the observed polarized morphologies in the disks, as recently shown by Kataoka et al. (2015) and Yang et al. (2016a).

The model of Kataoka et al. (2015) proposed that the polarized (sub)millimeter emission is produced by scattering of anisotropic radiation in dust grains with sizes of $\sim$ 100s μm. Yang et al. (2016a) included the scattering idea to dust grains in inclined disks. This study was expanded upon in Yang et al. (2016b), which used a semi-analytic model to combine polarization originating from both scattering and direct emission from grains aligned with a toroidal field. The polarization pattern strongly depends on the disk inclination (see Figure 3 in Yang et al. 2016b). For a 45° inclined disk, on one hand, the polarized emission due to scattering is concentrated along the disk major axis and the polarization vectors[8] are generally aligned with the minor axis. On the other hand, for disks with such inclination, the polarized direct emission is radial throughout the disk (i.e., the polarization vectors are perpendicular to the projected toroidal magnetic field). Despite the apparent differences between scattering and polarized dust grain emission, the current resolved polarization observations in disks are unable to distinguish clearly between them.

At a distance of 0.7 kpc (Moscadelli et al. 2009; Dzib et al. 2011), Cepheus A HW2 is one of the nearest high-mass YSOs. Its luminosity is about 1.3×10^4 $L_\odot$

[1] Instituto Argentino de Radioastronomía (CONICET), CCT La Plata, 1894, Villa Elisa, Argentina; manferna@gmail.edu
[2] Institute for Astrophysical Research, Boston University, Boston, MA 02215, USA
[3] Harvard-Smithsonian Center for Astrophysics, 60 Garden Street, Cambridge, MA 02138, USA
[4] Institut de Ciències de l'Espai, (CSIC-IEEC), Campus UAB, Carrer de Can Magrans S/N, E-08193 Cerdanyola del Valls, Catalonia, Spain
[5] Astronomy Department, University of Illinois, 1002 West Green Street, Urbana, IL 61801, USA
[6] Instituto de Astronomía, Universidad Nacional Autónoma de Mexico (UNAM), Apartado Postal 70-264, 04510 Mexico, DF, Mexico
[7] Institute of Astronomy & Department of Physics, National Tsing Hua University, No. 101, Section 2, Kuang-Fu Road, Hsinchu 30013, Taiwan

[8] These so-called *vectors* are not actually vectors but rather segments showing the orientation of the polarization plane.

([Evans et al. 1981](#)), which is that of a B0.5 main sequence star ([Rodriguez et al. 1994](#), although note that because this is not a main-sequence star some of the luminosity is due to accretion). [Patel et al. (2005)](#) found a rotating molecular and dusty 1-8 $M_\odot$ disk-like structure, with a radius of 330 AU ([Patel et al. 2005](#); [Brogan et al. 2007](#); [Torrelles et al. 2007](#); [Jiménez-Serra et al. 2009](#)). The dust continuum emission of this structure is elongated along the direction perpendicular to a thermal radio jet ([Rodriguez et al. 1994](#); [Hughes et al. 1995](#); [Curiel et al. 2002](#)) which has a 45° position angle (P.A., measured counterclockwise from north) and an ejection velocity of 500 km s^{-1} ([Curiel et al. 2006](#)). The radio jet is associated with part of a strong molecular outflow detected in different molecular tracers (H_2, CO and HCO^+). The outflow is precessing due to a multiple protostellar system harbored in the disk-like structure of HW2 ([Curiel et al. 2006](#); [Cunningham et al. 2009](#); [Zapata et al. 2013](#)).

Submillimeter and millimeter observations have detected two molecular clumps inside the HW2 gaseous disk ([Jiménez-Serra et al. 2007](#); [Brogan et al. 2007](#); [Comito et al. 2007](#); [Torrelles et al. 2007](#)) which may be interpreted as two separate hot cores ([Brogan et al. 2007](#); [Comito et al. 2008](#); [Jiménez-Serra et al. 2009](#)), or as gas heated by HW2 (i.e., the central protostar, [Torrelles et al. 2007](#)).

Other radio and millimeter sources in the Cepheus A region are probably harboring low/intermediate mass protostars. In particular, the protostellar source HW3c is detected at 0.8 mm and 1.3 mm at 3″5 south of HW2 ([Brogan et al. 2007](#); [Zapata et al. 2013](#)). HW3c is probably responsible for a prominent outflow running southwest of its position.

Polarimetric observations with the JCMT[9] at 850 μm (14″ angular resolution) show a centrosymmetric pattern of polarization vectors around the HW2/HW3c region (e.g., [Matthews et al. 2009](#); [Chrysostomou et al. 2003](#); [Curran & Chrysostomou 2007](#); also see [Glenn et al. 1999](#)). This pattern is broken along a 20″ depolarization band stretching across HW2 with a P.A.∼ 135° (i.e., a lane about 10 times the size of the disk-like structure). The plane of the sky magnetic field strength estimated from these observations is 6 mG ([Curran & Chrysostomou 2007](#)).

[Vlemmings et al. (2006)](#) measured magnetic field strengths (through H_2O Zeeman-splitting observations at 22.2 GHz) in the HW2 area ranging from 30 to 600 mG. These fields are strong enough to control the outflow dynamics ([Curran & Chrysostomou 2007](#)). Polarimetric observations of OH masers at 1665 MHz have a linear vector oriented at P.A.∼ 143° ([Bartkiewicz et al. 2005](#)). The resolution of the H_2O Zeeman-splitting observations and the JCMT polarimetric observations are drastically different (0″0005 versus 14″, respectively), which likely explains the very different field strengths. Finally, NIR K-band polarization observations at arcsecond resolution ([Jones et al. 2004](#)) report a centrosymmetric pattern in the arcminute scale, which may be interpreted as scattering due to the illumination by the central star(s). This pattern is centered at HW2, and is again disrupted in a southeast-northwest elongated lane

9 James Clerk Maxwell Telescope

crossing HW2. In this elongated lane, the polarization vectors show a roughly uniform direction, approximately aligned with the orientation of the lane itself.

In this contribution we present CARMA polarimetric millimeter observations partially resolving the circumstellar disk-like structure of Cepheus A HW2, which possibly harbors a cluster of high-mass protostars. These type of disk structures are generally large reservoirs of dense dust and gas, but their polarized emission has yet to be explored in detail. The paper is organized as follows. In Section 2, we describe our CARMA observations. In Section 3, we present the main results and the spatial distributions from the four Stokes parameters. In Section 4, we briefly discuss our findings. Finally, in Section 5, we summarize the main results.

2. OBSERVATIONS

The 1.3 mm CARMA observations toward Cepheus A HW2 were taken on three days: 2014 March 20, 21 and 2014 April 10. CARMA was in C configuration, with baselines ranging between 25 m and 310 m. The phase center of the telescope was R.A.(J2000.0)=$20^h56^m17\overset{s}{.}98$ and DEC(J2000.0)=$62°01'49\overset{''}{.}50$. For these observations, the receiver was tuned in Full Stokes mode, with four 500 MHz wide bands in each sideband, and a Local Oscilator frequency of 234.0112 GHz. As gain calibrators we used BLLAC and the quasar J0102+584. The bandpass calibrators were 3C454.3 and BLLAC. Leakages were solved using BLLAC and J0102+584. The leakage terms for each antenna were consistent from track to track, and the accuracy of their calibrations is within 0.1% ([Hull et al. 2014](#); [Hull & Plambeck 2015](#)). The absolute flux scale was determined from observations of MWC349 and BLLAC. We derive their fluxes from the CARMA dedicated quasar monitoring. A 15% uncertainty is estimated for the CARMA absolute flux calibration of the 230 GHz observations. The three tracks were calibrated using the Miriad package ([Sault et al. 1995](#)). Finally, we combined the data from the three tracks and produced images of the four Stokes products (I, Q, U and V). We also create a linear polarization intensity image ($p = \sqrt{Q^2 + U^2}$) and a polarization position angle image ($\chi = 0.5 \arctan U/Q$, with the arctan calculating the angle in the appropriate quadrant based on the signs of Q and U), constraining the polarization detection to those locations in which the linearly polarized emission has a signal-to-noise ratio (SNR) greater than 3 and the total intensity (Stokes I map) has SNR> 5. The synthesized beam of the naturally weighted images is 0″9 × 0″8 (P.A.= −48°), about 630 AU at 700 pc. The rms noise of the Stokes I map, which is limited by dynamic range, is 10.4 mJy beam^{-1} and for Stokes Q and U maps, which is limited by thermal-noise, is 1.2 mJy beam^{-1}.

3. RESULTS

Figure [1](#) shows a set of images of Cepheus A HW2 in full Stokes 1.3 mm continuum emission. Two bright sources are detected in Stokes I, known as HW2 and HW3c in the literature. One more feature is detected at the 3σ level, which is located 1″5 southeast of HW2; this feature is probably due to a peak in the noise spectrum. As reported in previous submillimeter observa-

tions (Patel et al. 2005; Torrelles et al. 2007), HW2 has two protrusions northwest and southeast of the protostellar location: SMA1 and SMA3. These features have been interpreted as possible protostellar cores in a tight cluster, but also have been suggested to be part of a more extended structure associated with the disk (Brogan et al. 2007). We measured a total integrated flux of 893 mJy for HW2. A 2D-Gaussian fit to its emission (Table 1) gives a structure with a deconvolved size $1''.21 \times 0''.82$ (850×575 AU at 700 pc). The P.A. of the HW2 millimeter emission is $135°$, which is orthogonally oriented to the thermal jet (P.A.= $44° \pm 4°$, Torrelles et al. 1996), thought to be the current ejection of the episodic precessing outflow (Cunningham et al. 2009; Zapata et al. 2013). The deconvolved size obtained from this fit is slightly larger than reported by Patel et al. (2005) from submillimeter observations, maybe due to a better sensitivity of CARMA to extended emission or differences in the spatial distribution of grains of different sizes. The peak location of the HW2 continuum source agrees with the protostar position derived in Curiel et al. (2006). HW3c is located $3''.5$ south of HW2. Its integrated 1.3 mm flux is 112 mJy, and a 2D-Gaussian fit shows that it is extended, with a deconvolved size of $1''.4 \times 0''.7$ (980×490 AU), and elongated in the north-south direction (P.A.= $2° \pm 10°$). Its peak position agrees with the position of the 1.3 cm radio source reported by Torrelles et al. (1996).

The images of the Stokes Q and V parameters are devoid of significant emission (Figure 1). However, the Stokes U image shows a clear detection ($> 7\sigma$) peaking at the HW2 location. Hence, the linear polarized intensity image (Figure 2) resembles the Stokes U emission distribution, and the polarized angle dispersion throughout HW2 is small. No other source was found to be polarized at a 3σ level (3 mJy beam^{-1}) within the field of view. The polarization fraction for HW3c is less than 1.9%. For HW2, we measured a total linear polarized intensity of 9 ± 1 mJy. The CARMA observations partially resolved the HW2 polarized emission, which spreads over two independent beams (5-6 beams at the 2σ level), with an average polarization fraction of $2.0\% \pm 0.4\%$. The morphology of the polarized emission shows two preferential elongations: one roughly aligned with the HW2 radio jet (northeast-southwest of the protostar location) and the other aligned with the major axis of the disk-like structure and due northwest. The average orientation of the electric field vectors ($57° \pm 6°$, measured counterclockwise from north) is deviated about $12°$ with respect to the HW2 radio jet and the disk normal directions (as shown in the left panel of Figure 2), but the deviation is smaller when considering the orientation of the northern lobe of the radio jet alone (P.A.= $50°$, Curiel et al. 2006). Moreover, the polarization vectors (P.A.= $57° \pm 6°$) are not exactly perpendicular to the dusty disk-like structure orientation (P.A.= $135°$).

4. MODELING AND DISCUSSION

In this section we discuss the nature of the polarimetric observations resolving the disk of Cepheus A HW2. First, we summarize the interpretations given to similar observations in other protostellar disks. It is of utmost importance to figure out the dominant polarization mechanism to analyze these data since each mechanism

provides different constraints on the disk's dust properties. We fit three polarization models to the data and comment on the results here.

4.1. *Previous polarized observations resolving disks of low-mass protostars*

In the disk of HL Tau, the polarization vectors are uniformly oriented and parallel to the minor axis, but the polarized emission stems mainly from an elongated region along the disk major axis (Stephens et al. 2014). Simple models for direct emission do not completely agree with the observations. This disagreement motivated new theoretical studies that showed that dust scattering is a viable alternative to explain the nature of the millimeter polarized emission of the HL Tau disk (Kataoka et al. 2015; Yang et al. 2016a; Kataoka et al. 2016). For the disk of L1527, the 1.3 mm CARMA polarization vectors are again uniformly oriented parallel to the minor axis of the disk, but the polarized emission seems to be along the same axis (Segura-Cox et al. 2015). These characteristics are expected for the direct emission of magnetically aligned grains threaded by a toroidal field in an edge-on disk (Yang et al. 2016b). However, the higher than average polarization fraction may also agree with the expectation for scattering in high-inclination disks. In the NGC1333 IRAS4A1 disk, the JVLA[10] polarized 8 mm/1 cm dust continuum emission (Cox et al. 2015) has been interpreted as possibly due to a mixture of magnetically aligned grains embedded in a toroidal magnetic field in the disk and dust scattering (Yang et al. 2016b). For the Class 0 disk IRAS 16293-2422 B (SMA[11] observations, Rao et al. 2014), the geometry of the disk (face-on) and the complex morphology of the 870 μm polarization vectors (swirled and curved) could be explained by a toroidal magnetic field model.

4.2. *Polarization vector models*

In order to better understand the nature of the polarized emission found in the disk-like structure of Cepheus A HW2, we test the orientation of the polarization vectors with three different models: grains aligned with a uniform magnetic field, grains aligned with a toroidal magnetic field, and polarization due to scattering. We fit each model to the observed orientations of the polarization vectors, but we did not fit the spatial distribution of the polarized emission nor the polarization fraction.

4.2.1. *Uniform magnetic field model*

The first model that we test is one with grains aligned with a uniform magnetic field threading the disk-like structure approximately along its major axis, which would cause a distribution of polarization vectors perpendicular to the field (i.e., northeast-southwest, along the minor axis). This distribution of vectors has the same morphology as the large-scale 850 μm polarization observations (Matthews et al. 2009), which traces a northeast-southwest parsec scale hour-glass shaped magnetic field, with a uniform distribution threading the central protostar(s), including HW2. In general, field lines are expected to be toroidal wrapped due to the rotation of

[10] Jansky Very Large Array
[11] Submillimeter Array

the gas in accretion disks, but it is feasible that in early stages and far from the inner disk, the magnetic field can be almost uniform.

We make a weighted linearly fit to the 1.3 mm polarization observations (orientations of the polarization vectors only) with a uniform field (Figure 3). The average fit orientation of the uniform field is given by a polarization vector set with P.A.= 56°, implying a magnetic field oriented with a P.A.= 146°. This is roughly consistent with the large-scale P.A. of 135°. As indicated by the residuals (mostly below the 3σ threshold of 18°), the model is a good match to the observed data.

4.2.2. *Toroidal magnetic field model*

The second model that we test is a simple one, with grains aligned with a toroidal magnetic field. Toroidal fields are proposed for MRI (magneto-rotational instability) dominated disks of low-mass protostars (e.g., Cho & Lazarian 2007). It is therefore an appropriate model to test against the CARMA observations.

We fit the observations (orientation of the polarization vectors only) allowing two free parameters: inclination (i) with respect to the plane of the sky (0° means face-on and 90° is edge-on) and position angle (more details of the model are given in the Appendix). The best fit gives $i = 45°$ and P.A.= 141° (Figure 4). A visual comparison with the uniform model fit clearly shows that the toroidal field is not a perfect match to the observations, with most of the residuals over 3σ, except for the region around the minor axis of the disk-like structure.

4.2.3. *Scattering in an inclined disk*

For the third model, we test inclination-induced scattering as the polarization mechanism (Yang et al. 2016a). We used a phenomenological model which is described in the Appendix. This is strictly a morphological comparison of the orientations of the polarization vectors for the model and data, and we neglect comparing the polarized intensity morphology. We neglect the latter to reduce the free parameters, given the limited amount of independent beams detected across the source. The best fit is found when the inclination is $i = 61°$ and the P.A.= 145° (left panel of Figure 5). Patel et al. (2005) estimated an inclination of 62° and a P.A. of 135° for the gaseous and dusty disk, which agrees with these results. The residuals of this model (right panel of Figure 5) are in general below the 3σ threshold, even lower (mean of the absolute residuals is 7°) than those obtained for the uniform magnetic field model (mean of the absolute residuals is 8°).

4.3. *Morphology of the polarized intensity*

Our models do not include the spatial distribution of the polarized intensity emission. If the morphology of the polarized emission is elongated along the major or minor axis of a disk, this can indicate that scattering or direct emission dominates the polarized emission, respectively (Yang et al. 2016b). A combination of both mechanisms produces also elongated polarized intensity along the major axis. In the case of HW2, the polarized intensity seems to be slightly elongated in the northeast-southwest direction (deconvolved size of $1''2 \pm 0''2 \times 1''0 \pm 0''2$ with a P.A. between 20° and 30°, depending on the vectors

between 2σ and 3σ are included or not), i.e., elongated across the minor axis of the disk-like structure. Since the elongation of the polarized intensity cannot be accurately determined from the present observations, we do not derive any convincing conclusion about the polarization mechanism only from the intensity distribution.

4.4. *Interpretation of the data*

The modeling of the orientations of the polarization vectors indicates a good match for the uniform magnetic field and scattering scenarios. It is clear from the residuals of Figures 3-5 that the toroidal field model is significantly worse than the other two models. Nevertheless, the polarized intensity shows a slight elongation along the minor axis of the disk-like structure, which could favor the direct emission mechanism from a toroidal field over the scattering.

We must make note of the caveats involved with this method of determining possible polarization mechanisms. First, CARMA is resolving the polarized emission only on a limited number of independent beams across the source. Both scattering and direct emission from grains aligned by a uniform magnetic field produce a similar pattern of vectors at the center of the disk-like structure, which explains the observations well, with residuals below the 3σ level. The lack of higher angular resolution and sensitivity also hinders the analysis of the elongation of the polarized intensity. When considering the emission over 3σ (Figure 2 left), it seems slightly elongated along the minor axis, but when considering the emission over 2σ (Figure 2 right), this preferential orientation is less clear. It is therefore complicated to use the elongation of polarization to distinguish between the direct emission and the scattering models.

Second, we are probably dealing with a massive disk-like structure that may be optically thick, particularly at the center. Note that our models are based on a 2D flatten disk and should be review to appropriately address how the optical depth modifies the polarization due to direct emission and/or scattering.

Finally, it is unclear that the millimeter emission toward HW2 comes entirely from a circumstellar accretion disk. The disk-like structure of HW2 is considered a dust and molecular rotating disk (Patel et al. 2005), but the dust emission could also contain a common envelope for the protostars, irregularities due to substructure of a multiple system, or even morphological disturbances produced by the action of the precessing jet. When present observations are improved, the assumed scattering model should probably be refined to include these effects.

The CARMA observations presented here cannot alone distinguish between the uniform magnetic field (direct emission) and the scattering scenarios, assuming the accretion disk dominates the dust emission in HW2. On one hand, the uniform magnetic field would imply the presence of a large-scale field possibly dragged by the dust and gas accretion into a flatten structure which has yet to wrap into a toroidal field, at least at large scales far away from the protostar(s). On the other hand, the scattering hypothesis would imply that grains have grown up to $\sim$ 10s of microns (Yang et al. 2016a; Kataoka et al. 2016). Grains grow very rapidly from $\sim$ 1 μm (ISM grain sizes) to several 10s of microns (grains in Class 0 and Class I disks, Kwon et al. 2009; Chiang et al. 2012;

Miotello et al. 2014). Since the age of HW2 has been estimated to be 10^4 yr (from its outflow dynamical time, Cunningham et al. 2009), this could be a new evidence of fast grain growth in dense environments. In the end, it may be a combination of polarization due to both mechanisms in play, although the hybrid (with a simple magnetic field configuration) model proposed by Yang et al. (2016b) may not perfectly explain the observations either.

5. SUMMARY AND CONCLUSIONS

We have reported the first resolved polarization observations of the disk-like structure of the high-mass protostar Cepheus A HW2. The 1.3 mm CARMA data show a partially resolved distribution of polarization vectors, suggesting an uniform morphology toward the center of the disk-like structure. The two likely mechanisms which could lead to the polarization of the millimeter emission are: (1) a magnetic field aligning the grains that emit polarized radiation, or (2) scattering from large enough dust grains (10s of microns). Fitting the observations with two phenomenological models (the uniform magnetic field threading the disk-like structure and the scattering in the inclined disk), we find both of these scenarios to be plausible and indeed, taking into account factors such as the opacity, a mixture of them may be expected.

If the main cause of the polarization is the grain alignment via magnetic forces, future intermediate resolution SMA observations could fill the gap between the CARMA ($1''$ resolution) and the previous JCMT ($20''$ resolution) millimeter and submillimeter data. This is crucial to make the link between the large scale hourglass shape morphology and the uniform vectors threading the most dense part of the disk-like structure. It is also clear from our fitting that the toroidal magnetic field does not match the CARMA observations. On the contrary, if the dominant cause of the polarized emission is scattering, the grains in the disk should have rapidly grown to sizes at least of the order of ~ 100 μm (probably in a few 10^4 yr, Kataoka et al. 2015; Yang et al. 2016a). This would add new evidence for quick grain growth taking place in dense disk-like structures, even in the adverse environment of a small cluster of massive protostars, where radiation or dynamical effects could restrict the growth of planetesimals. Both, multi-wavelength and sub-arcsecond angular resolution observations would give details to better distinguish which is the dominant mechanism.

REFERENCES

Andersson, B.-G., Lazarian, A., & Vaillancourt, J. E. 2015, ARA&A, 53, 501
Bartkiewicz, A., Szymczak, M., Cohen, R. J., & Richards, A. M. S. 2005, MNRAS, 361, 623
Beckwith, S. V. W., Henning, T., & Nakagawa, Y. 2000, Protostars and Planets IV, 533
Brogan, C. L., Chandler, C. J., Hunter, T. R., Shirley, Y. L., & Sarma, A. P. 2007, ApJ, 660, L133
Chiang, H.-F., Looney, L. W., & Tobin, J. J. 2012, ApJ, 756, 168
Cho, J., & Lazarian, A. 2007, ApJ, 669, 1085
Chrysostomou, A., Curran, R., Aitken, D., Jenness, T., & Davis, C. 2003, Ap&SS, 287, 161
Comito, C., Schilke, P., Endesfelder, U., Jiménez-Serra, I., & Martín-Pintado, J. 2007, A&A, 469, 207
—. 2008, Ap&SS, 313, 59
Cox, E. G., Harris, R. J., Looney, L. W., et al. 2015, ApJ, 814, L28
Cunningham, N. J., Moeckel, N., & Bally, J. 2009, ApJ, 692, 943
Curiel, S., Trinidad, M. A., Cantó, J., et al. 2002, ApJ, 564, L35
Curiel, S., Ho, P. T. P., Patel, N. A., et al. 2006, ApJ, 638, 878
Curran, R. L., & Chrysostomou, A. 2007, MNRAS, 382, 699
Dzib, S., Loinard, L., Rodríguez, L. F., Mioduszewski, A. J., & Torres, R. M. 2011, ApJ, 733, 71
Evans, II, N. J., Slovak, M. H., Becklin, E. E., et al. 1981, ApJ, 244, 115
Girart, J. M., Beltrán, M. T., Zhang, Q., Rao, R., & Estalella, R. 2009, Science, 324, 1408
Girart, J. M., Crutcher, R. M., & Rao, R. 1999, ApJ, 525, L109
Girart, J. M., Rao, R., & Marrone, D. P. 2006, Science, 313, 812
Glenn, J., Walker, C. K., & Young, E. T. 1999, ApJ, 511, 812

Gold, T. 1952a, Nature, 169, 322
—. 1952b, MNRAS, 112, 215
Hughes, V. A., Cohen, R. J., & Garrington, S. 1995, MNRAS, 272, 469
Hull, C. L. H., & Plambeck, R. L. 2015, Journal of Astronomical Instrumentation, 4, 1550005
Hull, C. L. H., Plambeck, R. L., Kwon, W., et al. 2014, ApJS, 213, 13
Jiménez-Serra, I., Martín-Pintado, J., Caselli, P., et al. 2009, ApJ, 703, L157
Jiménez-Serra, I., Martín-Pintado, J., Rodríguez-Franco, A., et al. 2007, ApJ, 661, L187
Jones, T. J., Woodward, C. E., & Kelley, M. S. 2004, AJ, 128, 2448
Kataoka, A., Muto, T., Momose, M., Tsukagoshi, T., & Dullemond, C. P. 2016, ApJ, 820, 54
Kataoka, A., Muto, T., Momose, M., et al. 2015, ApJ, 809, 78
Kwon, W., Looney, L. W., & Mundy, L. G. 2011, ApJ, 741, 3
Kwon, W., Looney, L. W., Mundy, L. G., Chiang, H.-F., & Kemball, A. J. 2009, ApJ, 696, 841
Lazarian, A. 2007, J. Quant. Spec. Radiat. Transf., 106, 225
Matthews, B. C., McPhee, C. A., Fissel, L. M., & Curran, R. L. 2009, ApJS, 182, 143
Miotello, A., Testi, L., Lodato, G., et al. 2014, A&A, 567, A32
Moscadelli, L., Reid, M. J., Menten, K. M., et al. 2009, ApJ, 693, 406
Patel, N. A., Curiel, S., Sridharan, T. K., et al. 2005, Nature, 437, 109
Pringle, J. E. 1981, ARA&A, 19, 137

Rao, R., Crutcher, R. M., Plambeck, R. L., & Wright, M. C. H. 1998, ApJ, 502, L75

Rao, R., Girart, J. M., Lai, S.-P., & Marrone, D. P. 2014, ApJ, 780, L6

Rodriguez, L. F., Garay, G., Curiel, S., et al. 1994, ApJ, 430, L65

Sault, R. J., Teuben, P. J., & Wright, M. C. H. 1995, in Astronomical Society of the Pacific Conference Series, Vol. 77, Astronomical Data Analysis Software and Systems IV, ed. R. A. Shaw, H. E. Payne, & J. J. E. Hayes, 433

Segura-Cox, D. M., Looney, L. W., Stephens, I. W., et al. 2015, ApJ, 798, L2

Stephens, I. W., Looney, L. W., Kwon, W., et al. 2013, ApJ, 769, L15

—. 2014, Nature, 514, 597

Testi, L., Birnstiel, T., Ricci, L., et al. 2014, Protostars and Planets VI, 339

Torrelles, J. M., Gomez, J. F., Rodriguez, L. F., et al. 1996, ApJ, 457, L107

Torrelles, J. M., Patel, N. A., Curiel, S., et al. 2007, ApJ, 666, L37

Vlemmings, W. H. T., Diamond, P. J., van Langevelde, H. J., & Torrelles, J. M. 2006, A&A, 448, 597

Yang, H., Li, Z.-Y., Looney, L., & Stephens, I. 2016a, MNRAS, 456, 2794

Yang, H., Li, Z.-Y., Looney, L. W., et al. 2016b, ArXiv e-prints, arXiv:1602.08196

Zapata, L. A., Fernández-López, M., Curiel, S., Patel, N., & Rodriguez, L. F. 2013, ArXiv e-prints, arXiv:1305.4084 [astro-ph.GA]

APPENDIX

In this section, we describe the expressions used to generate the synthetic polarization electrical vector images of the toroidal and scattering models (see Modeling and Discussion section). To make an E-vector image we first create its corresponding Stokes Q and U images (Miriad tasks IMGEN and MATHS) and convolve them with the CARMA synthesized beam (Miriad task CONVOL). We produce the E-vector image using Miriad task IMPOL. This image is then rotated by a position angle (task MATHS), since the Stokes Q and U images are originally obtained for P.A.= $0°$.

For the toroidal field model (radial E-vectors), we implement the following expressions for a 2D Cartesian coordinate system (x, y) in the plane of the sky, with the x- and y-axes along the major and minor axes of the disk-like structure respectively, and with the origin at the disk center:

$$Q = -D\left(x, y, i_2\right) \cdot \frac{x^2 - \left(y \cos i_2\right)^2}{x^2 + \left(y \cos i_2\right)^2} \quad , \tag{1}$$

$$U = -D\left(x, y, i_2\right) \cdot \frac{2xy \cos i_2}{x^2 + \left(y \cos i_2\right)^2} \quad , \tag{2}$$

where

$$D\left(x, y, i_1\right) = F_0 \cdot \left(\frac{\sqrt{x^2 + \left(y \cos i_1\right)^2}}{r_0}\right)^{-\alpha} \cdot e^{-\left(\sqrt{x^2 + \left(y \cos i_1\right)^2}/r_0\right)^{\beta}} \quad . \tag{3}$$

In the previous equations, $D\left(x, y, i\right)$ is a 2D function that is fitted to the Stokes I image (avoiding the $x = 0$, $y = 0$ point, which we set as the position observed Stokes I peak). In the fitting process, the free parameters are the exponents α and β, a characteristic radius r_0, the parameter F_0 (related to the central flux density of the disk-like structure) and the inclinations with respect to the plane of the sky i_1 and i_2. P.A.$_1$ and P.A.$_2$ (the angle of the disk in the plane of the sky counterclockwise from North) are also free parameters, but they do not appear explicitly in the above expressions, since they are implemented as a later rotation of the E-vector image. $D\left(x, y, i\right)$ is reminiscent of the standard viscous accretion disk model (Pringle 1981) used by other authors to fit the continuum emission of an accretion disk (e.g., Kwon et al. 2011; Yang et al. 2016a). The fit of Equation 3 to the Stokes I data is a sufficient representation of the disk-like structure emission, with residuals below the 3σ level. The fit values for the different parameters are presented in Table 2. After fitting the disk continuum emission the obtained values of F_0, r_0, α and β are fixed and used to create the Stokes Q and U. The obtained values of i_1 and P.A.$_1$ are discarded and left as two new free parameters (i_2 and P.A.$_2$) in Equations 1, 2, 4 and 5. By solving for i_2 and P.A.$_2$, we can find the best possible fit for each polarization model. This gives us an additional qualitative check on the models, since we can compare the fitted disk inclination and position angle from the orientations of the polarization vectors (i_2, P.A.$_2$) to that reported in the literature and the obtained from the fit of the Stokes I emission (i_1, P.A.$_1$).

The following mathematical expressions for the scattering model where inspired by equations (16) and (17) of Yang et al. (2016a). Our model is a phenomenological function and hence it is not based on physical principles. However, these expressions provide a representation of the effects of disk inclination on the orientations of the polarization vectors of scattered radiation shown in Figure 2 of Yang et al. (2016a).

$$Q = D\left(x, y, i_2\right) \cdot \left(1 - \sin^2 i_2 \cdot \frac{x^2}{x^2 + y^2}\right) \cdot \frac{x^2 \cos^2 i_2 - y^2}{x^2 \cos^2 i_2 + y^2} \quad , \tag{4}$$

$$U = D\left(x, y, i_2\right) \cdot \left(1 - \sin^2 i_2 \cdot \frac{x^2}{x^2 + y^2}\right) \cdot \frac{2xy \cos^2 i_2}{x^2 \cos^2 i_2 + y^2} \quad . \tag{5}$$

TABLE 1
Parameters of the Serpens South 3 mm continuum sources

Source	Right Ascension J2000	Declination J2000	Stokes I Peak (mJy beam^{-1})	Stokes I Flux (mJy)	P$^{(a)}$ (mJy)	P%$^{(b)}$ (%)	P.A.$^{(c)}$
HW2	$22^h56^m17\overset{s}{.}989$	$62°01'49\overset{''}{.}60$	423 ± 10	863 ± 20	9 ± 1	2.0 ± 0.4	57 ± 6
HW3c	$22^h56^m17\overset{s}{.}976$	$62°01'46\overset{''}{.}10$	68 ± 10	160 ± 6	$\cdots$	$\cdots$	$\cdots$

Note. —
[a] Polarized intensity flux.
[a] Fraction of polarized emission (percentage average).
[c] Position angles of the polarized emission are measured counterclockwise.

TABLE 2
Parameters obtained from the
Stokes I fit

Parameter	Fit
$F_0{}^{(a)}$	2.5×10^{-4} Jy pixel^{-1}
r_0	$1\overset{''}{.}0$
α	1.2
β	1.6
i_1	$51°$
P.A.$_1$	$142°$

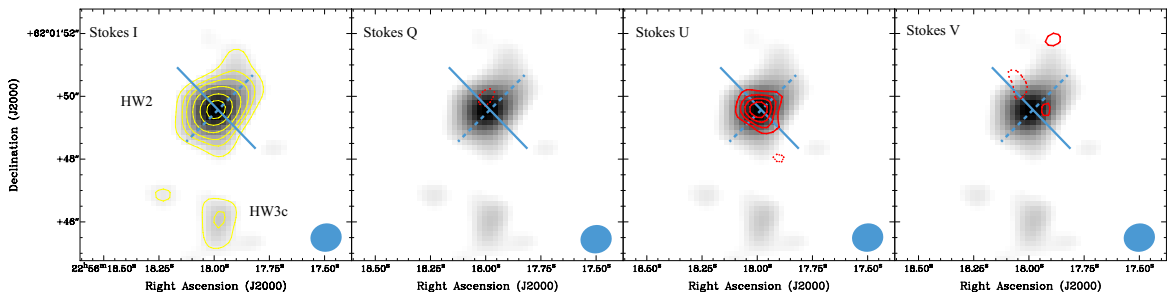[a] The size of a pixel is $0\overset{''}{.}05$.

Fig. 1.— Images of the 1.3 mm continuum emission for Cepheus A in each of the four Stokes parameters taken with CARMA. The Stokes I emission appears in the four panels in grayscale. Overlayed yellow contours for the Stokes I are at -3, 3, 6, 9, 15, 25, 35 $\times\sigma$, where $\sigma = 10$ mJy beam^{-1} is the rms noise level of the image. For Stokes Q, U and V, red contours are at -3, 3, 4, 5, 6 $\times\sigma$, where $\sigma = 1$ mJy beam^{-1} is the rms noise level of these three images. The two main sources in the field are labeled in the Stokes I image. The orientation of the disk-like structure ($P.A. \sim 135°$) and the jet of HW2 ($P.A. \sim 45°$) are marked with blue lines (dashed and solid, respectively). The synthesized beam is shown in the bottom right corner.
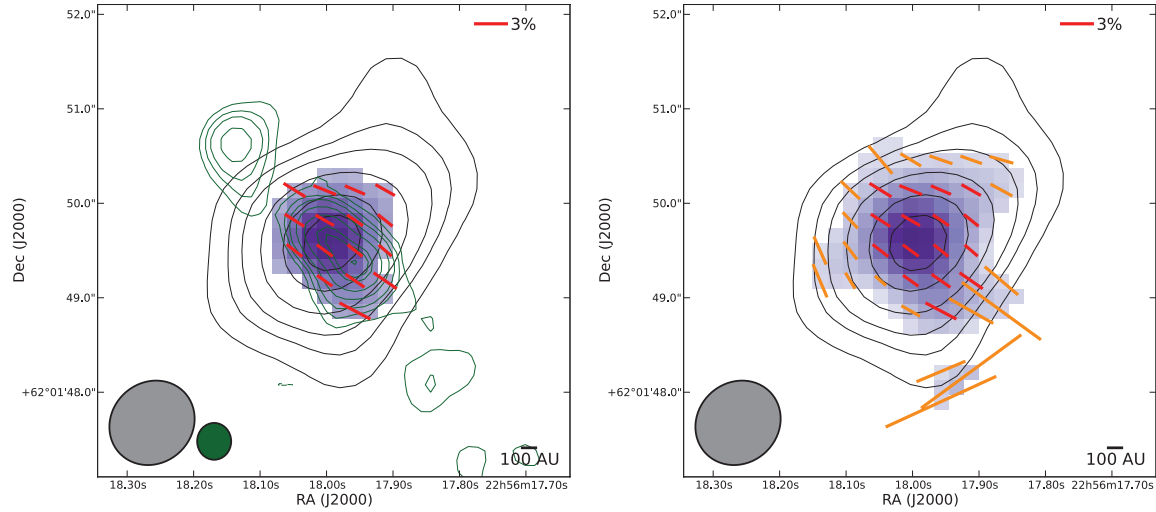
FIG. 2.— **Left:** Polarimetric map (polarization E-vectors) of the Cepheus A HW2 disk-like structure. Fractional polarization red vectors over 3σ displayed. Black contours are Stokes I data with the same levels as in Figure 1. Green contours correspond to the VLA C band continuum emission showing the radio jet at -6, -3, 3, 6, 10, 20, 40, 80, 100 and 140 times the rms noise level of the 6 cm radio map, 28 μJy beam^{-1}) associated with the HW2 massive protostar. Color scale shows the polarized intensity over 3σ. The synthesized beam of both CARMA (grey) and VLA (green) observations are shown at the bottom left corner. **Right:** Same map as in left panel but including orange vectors between 2σ and 3σ. The polarized intensity (color scale) also shows emission over 2σ.
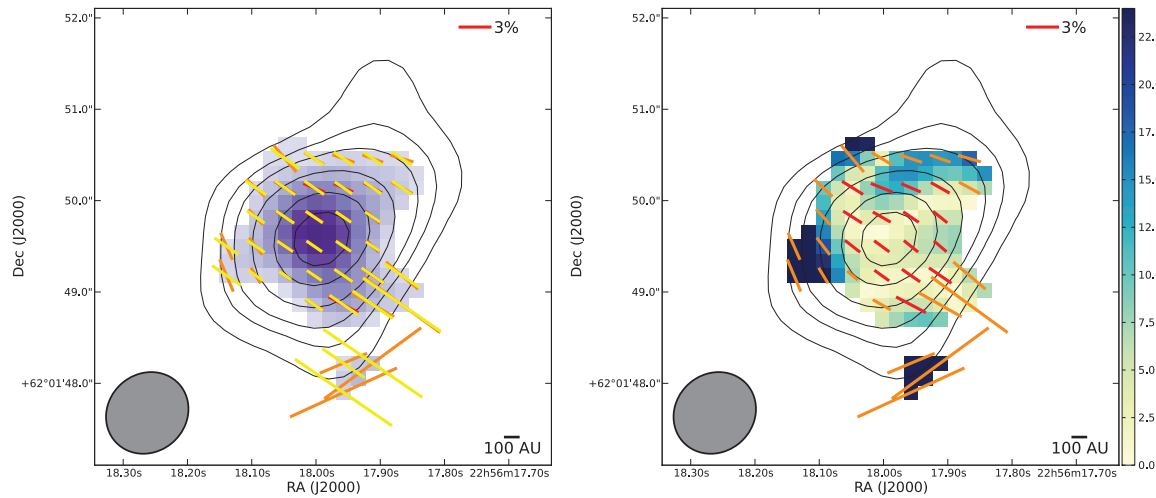

FIG. 3.— **Left:** Uniform magnetic field model (yellow polarization E-vectors) compared with the 1.3 mm polarimetric observations (orange and red vectors are CARMA detections between 2σ and 3σ and $> 3\sigma$, respectively). Contours are Stokes I data with the same levels as in Figure 1. Color scale shows the polarized intensity over 2σ. **Right:** The absolute value of the residuals between the observed and the modeled orientations of the polarization vectors (color scale, in degrees). The mean rms level of the E-vectors is 6°. Contours are Stokes I data with the same levels as in Figure 1. Vectors are as in the right panel of Figure 2.
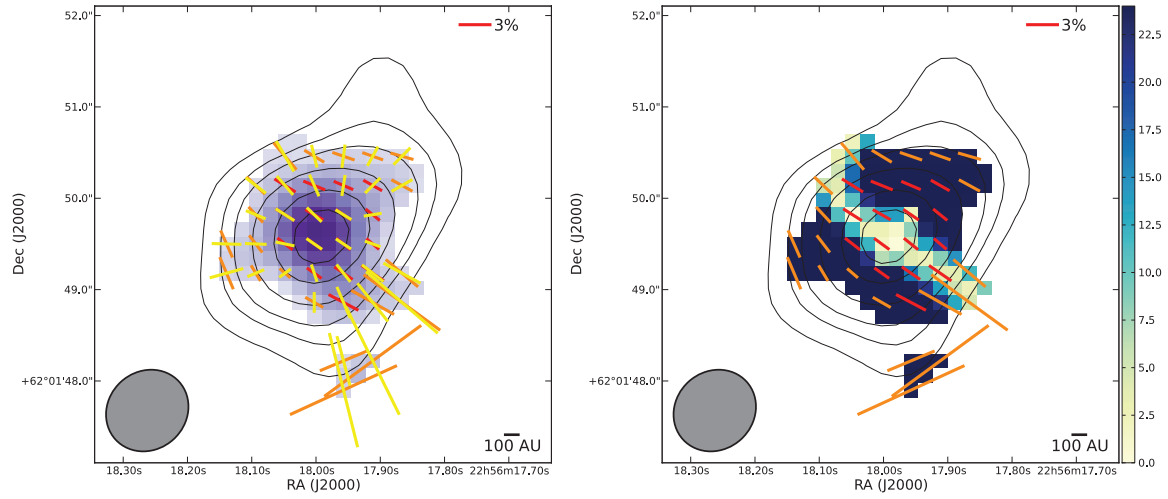
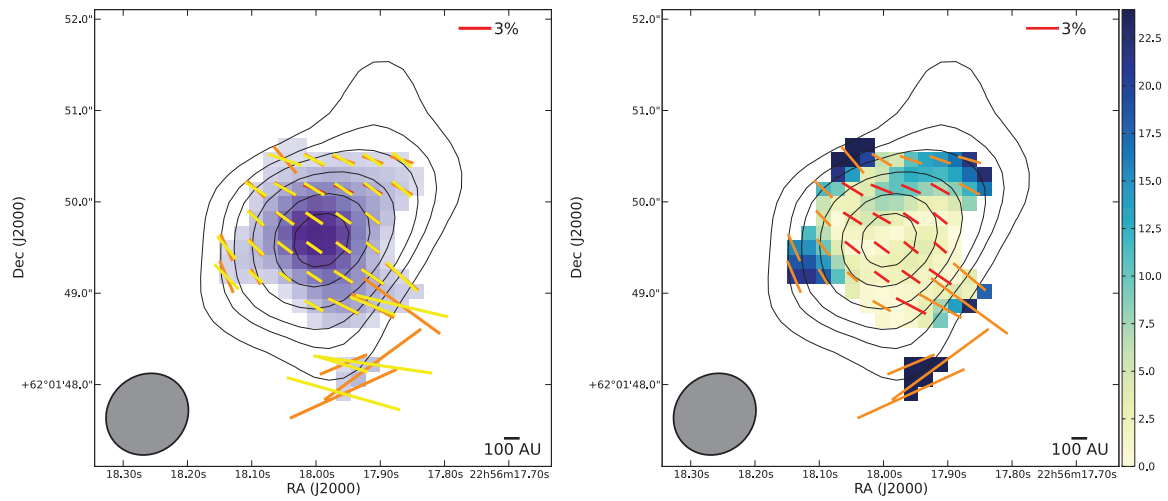Fig. 4.— Same as Figure 3, except for the toroidal magnetic field model (see text).

Fig. 5.— Same as Figure 3, except for the scattering model (see text).